Volume 10 | Number 36 | 28 September 2019 | Pages 8275–8492

Chemical Science

rsc.li/chemical-science

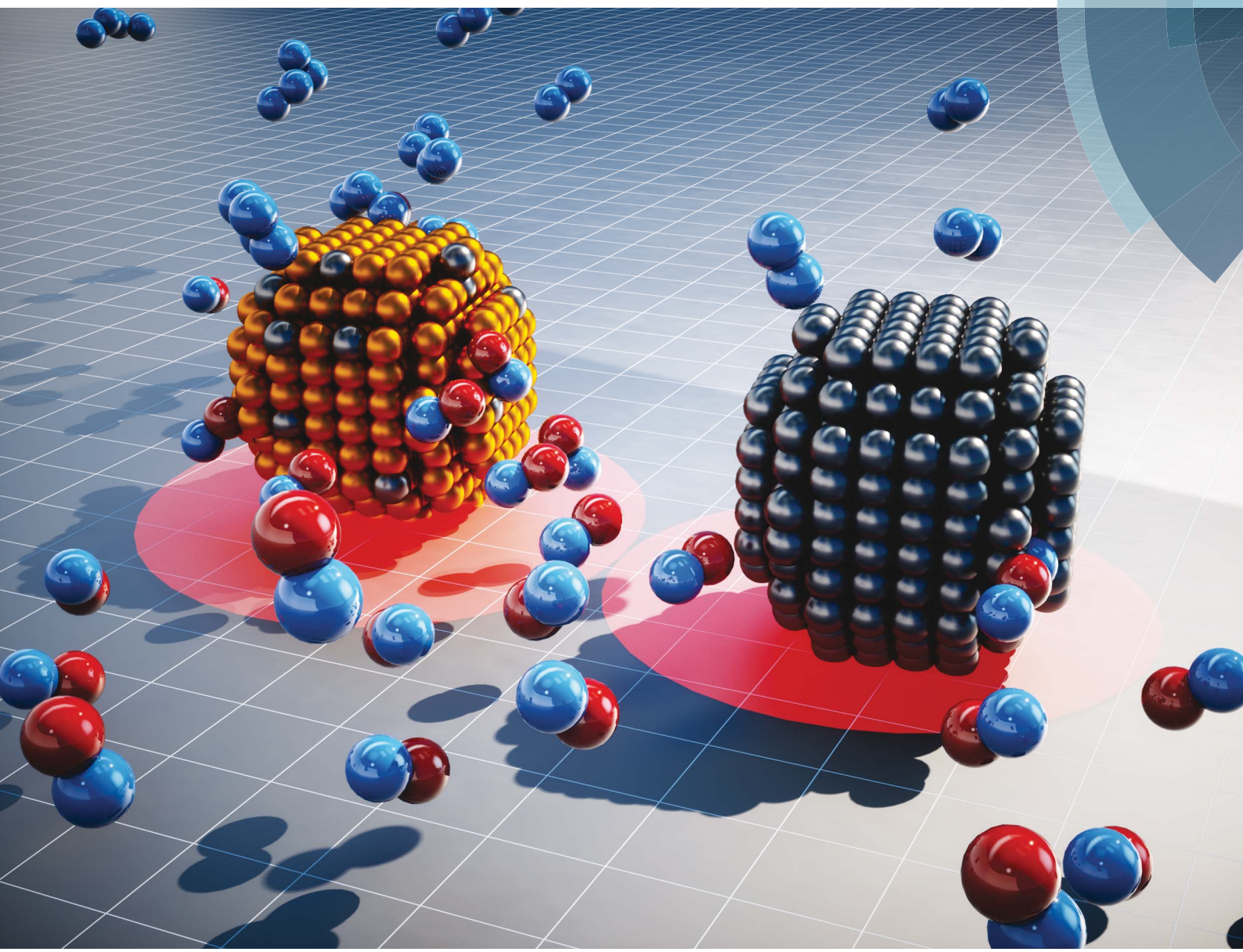

ISSN 2041-6539

ROYAL SOCIETY OF CHEMISTRY | Celebrating IYPT 2019

EDGE ARTICLE
Shinya Furukawa *et al.*
A Cu–Pd single-atom alloy catalyst for highly efficient NO reduction

Chemical Science

EDGE ARTICLE

View Article Online
View Journal | View Issue

Cite this: *Chem. Sci.*, 2019, **10**, 8292

All publication charges for this article have been paid for by the Royal Society of Chemistry

Received 27th June 2019
Accepted 5th August 2019

DOI: 10.1039/c9sc03172c

rsc.li/chemical-science

A Cu–Pd single-atom alloy catalyst for highly efficient NO reduction†

Feilong Xing,[a] Jaewan Jeon,[a] Takashi Toyao,[ab] Ken-ichi Shimizu[ab] and Shinya Furukawa*[ab]

A series of Cu–Pd alloy nanoparticles supported on Al_2O_3 were prepared and tested as catalysts for deNO_x reactions. XRD, HAADF-STEM, XAFS, and FT-IR analyses revealed that a single-atom alloy structure was formed when the Cu/Pd ratio was 5, where Pd atoms were well isolated by Cu atoms. Compared with Pd/Al_2O_3, Cu_5Pd/Al_2O_3 exhibited outstanding catalytic activity and N_2 selectivity in the reduction of NO by CO: for the first time, the complete conversion of NO to N_2 was achieved even at 175 °C, with long-term stability for at least 30 h. High catalytic performance was also obtained in the presence of O_2 and C_3H_6 (model exhaust gas), where a 90% decrease in Pd use was achieved with minimum evolution of N_2O. Kinetic and DFT studies demonstrated that N–O bond breaking of the $(NO)_2$ dimer was the rate-determining step and was kinetically promoted by the isolated Pd.

Introduction

The reactions of nitric oxide (NO) have garnered intense interest from researchers in the human health,[1] and bioinorganic,[2] industrial,[3] and environmental chemistry fields.[4] Specifically, NO removal has long been studied as an indispensable process for exhaust-gas purification.[5] Platinum-group metals (PGMs) such as Pt, Pd, and Rh are known to be efficient catalysts for the reduction of NO using CO,[6,7] H_2,[8] NH_3,[9] and hydrocarbons[10] as reductants. The recent challenges in this field involve developing catalytic systems that function (1) at low temperatures under cold-start conditions,[11] (2) with minimum use of PGMs,[12,13] and (3) without emitting N_2O,[14–16] which is a potent greenhouse gas.[17] These issues have been individually studied using different materials. The development of a single material that enables (1)–(3) is therefore highly desirable. To the best of our knowledge, no such material has been reported. In particular, achieving both (1) and (3) is difficult because N_2O reduction to N_2 on PGMs requires relatively high temperatures (>300 °C).[18] Therefore, an appropriate catalyst design is needed to obtain not only outstanding catalytic activity toward NO reduction but also high selectivity to N_2 with minimal incorporation of PGMs.

A promising approach that overcomes these challenges is the single-atom alloying concept,[19] which is relevant to single-atom chemistry.[20,21] The dilution of PGM atoms with less active metal atoms not only substantially reduces the use of PGMs but also enables drastic modification of the electronic and geometric structures for enhanced catalysis.[22] For example, the isolation of Pt or Pd with group 11 metals (Au, Ag, and Cu) enables molecular transformations that hardly proceed in the absence of single-atom alloying, such as selective hydrogenation,[23–27] formic acid dehydrogenation,[28] and hydrosilylation.[29] In these systems, the group 11 metals act as inert elements but modify the electronic and geometric factors of the PGM and, thus, its catalytic properties. Conversely, for NO reduction, the group 11 elements are known to be capable of NO activation.[30–32] Therefore, applying the single-atom alloying concept to NO reduction systems should provide an unprecedented synergistic effect for efficient NO conversion.

In this study, we focused on Cu as a main component because of its intrinsic activity toward NO reduction and its high earth abundance. We found that $Cu–Pd/Al_2O_3$ (Cu/Pd = 5) acts as a highly efficient catalyst for NO reduction at low temperatures (>150 °C), without generating N_2O emissions. Herein, we report both an innovative catalytic system for efficient NO reduction and novel catalytic chemistry of single-atom alloys.

Experimental details

Catalyst preparation

Boehmite (γ-AlOOH) was supplied by SASOL Chemicals. γ-Al_2O_3 was prepared by the calcination of boehmite at 900 °C for 3 h. Pd/Al_2O_3 (Pd: 2 wt%) and $Cu–Pd/Al_2O_3$ (Cu: 6 wt%, Cu/Pd = 1) were prepared by a conventional impregnation method. The γ-Al_2O_3 support was added to a vigorously stirred aqueous

[a]Institute for Catalysis, Hokkaido University, N-21, W-10, Sapporo 001-0021, Japan. E-mail: furukawa@cat.hokudai.ac.jp; Fax: +81-11-706-9163

[b]Elements Strategy Initiative for Catalysts and Batteries, Kyoto University, Katsura, Kyoto 615-8520, Japan

† Electronic supplementary information (ESI) available: Details of characterization, kinetic analysis, and DFT calculations. See DOI: 10.1039/c9sc03172c

solution containing $Pd(NH_3)_2(NO_2)_2$ (Kojima Chemicals, 4.765 wt% in HNO_3) and/or $Cu(NO_3)_2 \cdot 3H_2O$ (Sigma-Aldrich, 99%), followed by stirring for 3 h at room temperature (50 ml H_2O per gram of Al_2O_3). The mixture was dried under a reduced pressure at 50 °C, followed by reduction under flowing H_2 (30 ml min^{-1}) at 400 °C (Pd) or 800 °C (CuPd) for 1 h. The Cu/Al_2O_3 (Cu: 6 wt%) and Cu–Pd/Al_2O_3 (Cu: 6 wt%, Cu/Pd = 3 and 5) catalysts were prepared by a deposition–precipitation method using urea. The γ-Al_2O_3 support was added to a vigorously stirred aqueous solution of $Cu(NO_3)_2 \cdot 3H_2O$ (50 ml H_2O per gram of Al_2O_3). Then, an aqueous solution of urea (Kanto, 99%) was added dropwise to the stirred mixture at room temperature (urea/Cu = 30). The mixture was sealed with a plastic film and kept with stirring at 70 °C for 10 h. After completing the precipitation of $Cu(OH)_2$, the supernatant was decanted and the resulting crude product was washed with deionized water three times, followed by drying under a reduced pressure at 50 °C and calcination at 500 °C for 1 h. For Cu/Al_2O_3, the resulting CuO/Al_2O_3 was reduced under flowing H_2 at 400 °C for 1 h. For Cu–Pd/Al_2O_3 (Cu/Pd = 3 and 5), the resulting CuO/Al_2O_3 was used for successive impregnation of Pd in a similar fashion to that mentioned above. The resulting Pd–CuO/Al_2O_3 was reduced under flowing H_2 at 400 °C for 1 h.

Reaction conditions

The catalyst (0.05 g) diluted with quartz sand (1.95 g, Miyazaki Chemical, 99.9%) was treated under flowing hydrogen (50 ml min^{-1}) at 400 °C for 0.5 h prior to the catalytic reactions. NO reduction by CO was performed in a fixed-bed continuous flow system by feeding NO (5000 ppm), CO (5000 ppm), and He (balance) with a total flow rate of 96 ml min^{-1} (GHSV = 80 000 h^{-1}). The gas phase was analyzed using an online thermal conductivity detection gas chromatograph (Shimadzu GC-8A, column: SHINWA SHINCARBON ST) located downstream. A stability test was done using twice the amount of catalyst (0.10 g) under similar conditions (GHSV = 40 000 h^{-1}). After a time-on-stream of 24 h, the catalyst was regenerated by flowing hydrogen (50 ml min^{-1}) at 400 °C for 0.5 h, followed by continuing the catalytic run. A kinetic study was performed by changing the concentration of NO and CO between 0.3 and 0.6% with that of the counterpart fixed at 0.5%. The reaction temperature was maintained at 150 °C so that NO conversion did not exceed 30%, and the reaction rate (mol s^{-1} $mol_{Pd}{}^{-1}$) was calculated on the basis of NO conversion. NO + CO + O_2 and NO + CO + O_2 + C_3H_6 reactions were performed under stoichiometric conditions as follows: NO (5000 ppm), CO (10 000 ppm), O_2 (2500 ppm), He (balance) with a total flow rate of 96 ml min^{-1} (GHSV = 80 000 h^{-1}), and NO (5000 ppm), CO (5000 ppm), O_2 (5625 ppm), C_3H_6 (1250 ppm), and He (balance) with a total flow rate of 96 ml min^{-1} (GHSV = 80 000 h^{-1}), respectively.

Characterization

The crystal structure of the prepared catalyst was examined by powder X-ray diffraction (XRD) using a Rigaku MiniFlex II/AP diffractometer with Cu Kα radiation. High-angle annular dark field scanning transmission electron microscopy (HAADF-STEM) was carried out using a JEOL JEM-ARM200 M microscope equipped with an energy dispersive X-ray (EDX) analyzer (EX24221M1G5T). STEM analysis was performed at an accelerating voltage of 200 kV. To prepare the TEM specimen, all samples were sonicated in ethanol and then dispersed on a Mo grid supported by an ultrathin carbon film.

The Fourier-transformed infrared (FT-IR) spectra of adsorbed CO were obtained with a JASCO FTIR-4200 spectrometer equipped with an MCT detector in transmission mode (resolution 4 cm^{-1}). The samples were prepared as self-supporting wafers (2.0 cm diameter, <0.5 mm thickness) and were placed inside an IR cell with CaF_2 windows. A custom glass manifold was connected to the cell to control the gas for pretreatment and the amount of CO introduced. The cell was first purged with He, and the sample was reduced under flowing hydrogen (50 ml min^{-1}) at 400 °C for 30 min. After reduction, the wafer was cooled to 40 °C under flowing He. The wafer was exposed to CO (0.5%) and He (balance) with a total flow rate of 50 ml min^{-1} for 20 min. After the CO exposure, He was flowed for 5 min to remove the gas phase and weakly adsorbed CO, followed by IR spectral measurements.

X-ray absorption fine structure (XAFS) spectra were recorded on the BL14B2 station at SPring-8 of the Japan Synchrotron Radiation Research Institute. A Si(311) double-crystal monochromator was used. Energy calibration was performed using Pd foil. The spectra were recorded at the edges of Pd K in a transmission mode at room temperature. The pelletized sample was pre-reduced with H_2 at 400 °C for 0.5 h, and then sealed in a plastic pack under a N_2 atmosphere together with an ISO A500-HS oxygen absorber (Fe powder). The obtained XAFS spectra were analyzed using Athena and Artemis software ver. 0.9.25 included in the Demeter package. The Fourier transformation of the k^3-weighted EXAFS from k space to R space was performed over a k range of 3.0–15 $Å^{-1}$. Some of the Fourier-transformed EXAFS spectra in the R range of 1.2–3.0 Å were inversely Fourier transformed, followed by an analysis using a usual curve fitting method in a k range of 3–15 $Å^{-1}$. The back-scattering amplitude or phase shift parameters were simulated with FEFF 6L and used to perform the curve fitting procedure. For Pd–Cu scattering, intermetallic Cu_3Pd with a $Pm\bar{3}m$ structure was considered for the FEFF simulation. The amplitude reduction factor ($S_0{}^2$) of Pd was determined to be 0.775 by fitting the spectra of Pd black and then used for fitting of other EXAFS spectra.

Computational details

Periodic DFT calculations were performed using the CASTEP code[33] with Vanderbilt-type ultrasoft pseudopotentials[34] and the Perdew–Burke–Ernzerhof exchange–correlation functional based on the generalized gradient approximation.[35] The plane-wave basis set was truncated at a kinetic energy of 350 eV, and a Fermi smearing of 0.1 eV was utilized. Dispersion corrections were considered using the Tkatchenko–Scheffler method with a scaling coefficient of $s_R = 0.94$ and a damping parameter of $d = 20$.[36] The reciprocal space was sampled using

a *k*-point mesh with a spacing of typically 0.04 $Å^{-1}$, as generated by the Monkhorst–Pack scheme.[37] Geometry optimization was performed on supercell structures using periodic boundary conditions. The surface was modeled based on Cu(211)-(2 × 3) (for NO and N_2O related reactions), Cu(111)-(2 × 2) (for CO oxidation), and Cu(111)-(3 × 3) (for N_2O decomposition) slabs that were six atomic layers thick with 13 Å of vacuum spacing. The convergence criteria for structural optimization and energy calculation were set to (a) an SCF tolerance of 1.0×10^{-6} eV per atom, (b) an energy tolerance of 1.0×10^{-5} eV per atom, (c) a maximum force tolerance of 0.05 eV $Å^{-1}$, and (d) a maximum displacement tolerance of 1.0×10^{-3} Å. The transition state search was performed using the complete linear synchronous transit/quadratic synchronous transit (LST/QST) method.[38,39] Linear synchronous transit maximization was performed, followed by energy minimization in the directions conjugate to the reaction pathway. The approximated TS was used to perform QST maximization with conjugate gradient minimization refinements. This cycle was repeated until a stationary point was found. Convergence criteria for the TS calculations were set to root-mean-square forces on an atom tolerance of 0.10 eV $Å^{-1}$.

Results and discussion

The monometallic Cu (6 wt%) and Pd (2 wt%) and the bimetallic Cu–Pd (Cu: 6 wt%, Cu/Pd = 1, 3, or 5; hereafter, Cu_xPd, $x = 1$, 3, or 5) catalysts were prepared using γ-Al_2O_3 as a support by deposition–precipitation and/or impregnation methods. X-ray diffraction (XRD) patterns of the prepared catalysts revealed that Cu–Pd solid-solution alloy phases with bimetallic compositions similar to the metal ratio in the feed were formed (Fig. S1† and Table 1).

The crystallite sizes estimated using Scherrer's equation were 3–4 nm for all of the catalysts. Fig. 1a and b show a high-angle annular dark field scanning transmission electron microscopy (HAADF-STEM) image of Cu_5Pd/Al_2O_3 and the size distribution of the nanoparticles, respectively. A relatively narrow size distribution between 2 and 6 nm with an area-weighted mean diameter of 4.2 nm was obtained, consistent with the crystallite size estimated by XRD (Table 1).

The energy-dispersive X-ray spectroscopy (EDS) analysis of a single nanoparticle revealed that the Cu and Pd atoms comprising the nanoparticle were homogeneously dispersed (Fig. 1c). The high-resolution HAADF-STEM image shows an fcc

Table 1 Detailed information on the catalyst prepared in this study

	Pd	CuPd	Cu_3Pd	Cu_5Pd	Cu
Pd loading (wt%)	2.0	10.1	3.4	2.0	0
Cu loading (wt%)	0	6.0	6.0	6.0	6.0
Cu fraction in the catalyst	0	0.50	0.75	0.83	1.0
Cu fraction in particles	0	0.44	0.72	0.89	1.0
Crystallite size/nm[a]	3.2	3.3	3.8	3.8 (4.2)[b]	4.0

[a] Estimated from Scherrer's equation using a Scherrer constant of 0.477 for the area-weighted mean diameter. [b] Area-weighted mean diameter obtained from TEM images.

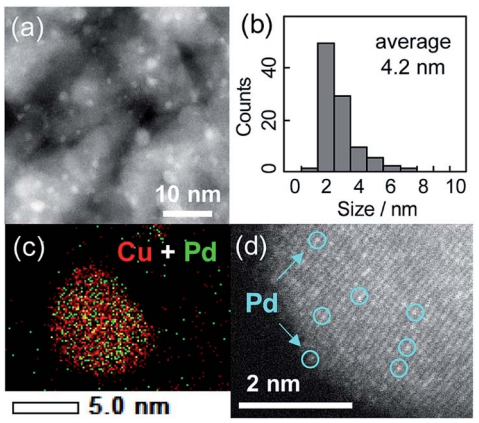

Fig. 1 (a) HAADF-STEM image of Cu_5Pd/Al_2O_3 and (b) size distribution of the nanoparticles. (c) Elemental map of the Pd + Cu overlayer, as acquired by EDS. (d) High-resolution image of a single nanoparticle.

crystal structure viewed along the [100] direction, consistent with the formation of a solid-solution alloy (Fig. 1d). Moreover, the isolation of Pd atoms by Cu was indicated by the presence of atoms with distinct Z contrasts. Note that the corresponding HAADF-STEM image of Cu/Al_2O_3 showed a weak and uniform Z contrast compared with that of Cu_5Pd/Al_2O_3 (Fig. S2†).

The degree of Pd isolation was further investigated by Fourier-transform infrared (FT-IR) and extended X-ray absorption fine structure (EXAFS) analyses (Fig. 2). As shown in Fig. 2a, the FT-IR spectra of CO adsorbed onto Pd/Al_2O_3 exhibited absorption peaks assigned to the stretching vibration of C═O

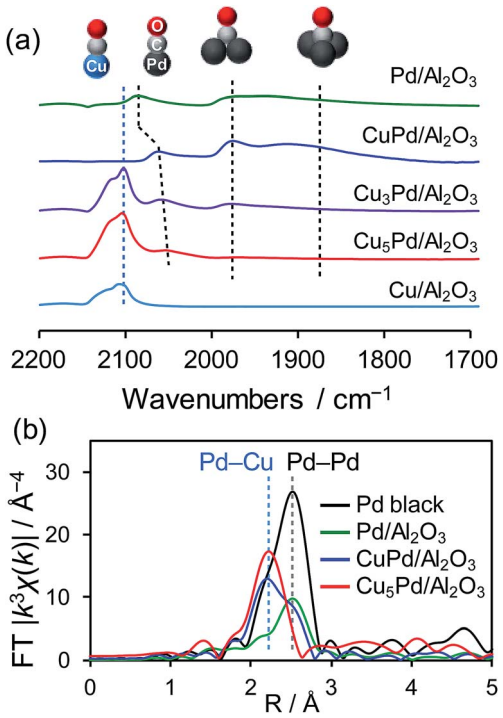

Fig. 2 (a) FT-IR spectra of CO adsorbed on the prepared catalysts. (b) Fourier transforms of the Pd K-edge EXAFS spectra of the Pd-based catalysts.

adsorbed on top (2086 cm^{-1}), bridge (1975 cm^{-1}), and hollow sites (~1880 cm^{-1}).[40] Similar absorption peaks were observed for $CuPd/Al_2O_3$, suggesting that the Pd–Pd ensembles largely remain even after 1 : 1 alloying. For Cu-rich samples, an absorption band assignable to CO adsorbed on metallic Cu was also observed at 2100 nm^{-1}.[41] The peak intensities for the bridge and hollow CO substantially decreased and disappeared in the spectra of Cu_3Pd/Al_2O_3 and Cu_5Pd/Al_2O_3, respectively, indicating that Pd atoms at the surface were isolated upon 5 : 1 alloying.

There remained a weak absorption band for linear CO on Pd in the spectrum for Cu_5Pd/Al_2O_3, suggesting that the isolated Pd atoms are also present at the surface. Fig. 2b shows the Fourier transforms of the Pd K-edge EXAFS spectra of the Pd-based catalysts (the X-ray absorption near edge structure spectra, raw EXAFS oscillations, curve-fitting, and summary of EXAFS curve fitting are shown in Fig. S3–S5 and Table S1,† respectively). $CuPd/Al_2O_3$ showed both Pd–Pd and Pd–Cu bonds, while Cu_5Pd/Al_2O_3 exclusively showed Pd–Cu bonds, suggesting that the Pd atoms in the bulk were also isolated by Cu upon 5 : 1 alloying. Thus, small Cu–Pd nanoparticles with a single-atom alloy structure were successfully formed on the Al_2O_3 support. Considering the limited sensitivity of EXAFS and FT-IR, we cannot completely exclude the presence of Pd–Pd interaction. However, only a small number of Pd–Pd sites, if any, seem not to contribute to the overall catalytic performance.

We next tested the catalytic activity of Cu_xPd/Al_2O_3 in NO reduction by CO (GHSV = 80 000 h^{-1}), as a model reaction for exhaust-gas purification. Fig. 3a shows the NO conversion to N_2 (C_{N_2}) for the prepared catalysts as a function of reaction temperature. Here, C_{N_2} was obtained by multiplying the NO conversion and the N_2 selectivity (Fig. S6†). Pd/Al_2O_3 gave the lowest C_{N_2}, because of the poor N_2 selectivity <40% (Fig. S6b†).

Cu/Al_2O_3 exhibited a higher C_{N_2} than Pd/Al_2O_3 because of its much higher N_2 selectivity (Fig. S6b†). $CuPd/Al_2O_3$ showed a C_{N_2} trend similar to that of Cu/Al_2O_3 because of the consequence of increased NO conversion and decreased N_2 selectivity (Fig. S6†). Thus, the 1 : 1 alloy of Cu and Pd gave an insufficient catalytic performance for selective NO reduction. Interestingly, however, both NO conversion and N_2 selectivity increased when the alloying ratio was increased to 3 : 1 and 5 : 1 (Fig. S6†), which resulted in great enhancements in C_{N_2} (Fig. 3a). NO was completely converted to N_2 over Cu_5Pd/Al_2O_3 without generating N_2O emissions even at 200 °C, where Pd showed a C_{N_2} of only 5%. Notably, on going from CuPd to Cu_5Pd, the catalytic activity increased even though the Pd content was decreased to 1/5 (Table 1). Therefore, a specific synergistic effect between Cu and Pd likely contributed to the unique properties of the single-atom alloy catalyst. We emphasize that using an excess amount of Pd/Al_2O_3 (0.50 g) with 10 times the equimolar Pd included in Cu_5Pd/Al_2O_3 (labeled as Pd × 10) still resulted in poor performance (Fig. 3b), highlighting the outstanding performance of the single-atom alloy catalyst. We also tested the long-term stability of Cu_5Pd/Al_2O_3 in NO reduction by CO under standard conditions (GHSV = 40 000 h^{-1}), where 100% C_{N_2} was maintained at 175 °C. Although a number of bimetallic catalysts for NO reduction have been reported thus far,[12–16,42–48] to the best of our knowledge, the present work represents the first success in complete NO_x removal at a temperature less than 200 °C. At 150 °C, although C_{N_2} decreased slightly at the initial stage because of N_2O formation, it recovered after a short H_2 treatment. This result implies that the accumulation of oxygen species at the catalyst surface triggers the loss of N_2 selectivity and that the catalytic performance could be recovered under rich conditions. We next examined the catalytic performance of Cu_5Pd/Al_2O in NO reduction in the presence of O_2 and O_2 + C_3H_6; these conditions more closely resemble those encountered in practical use. Cu/Al_2O_3 delivered poor performance under NO + CO + O_2 conditions. By contrast, Cu_5Pd/Al_2O exhibited much higher performance than Cu/Al_2O and Pd/Al_2O. Notably, Cu_5Pd/Al_2O still exhibited a performance better than or comparable to "Pd × 10" even in the presence of O_2 or O_2 + C_3H_6, respectively (Fig. 3b and S7;† a comparison with temperature dependence and T_{50} is presented in Fig. S7†). Furthermore, N_2O evolution was sufficiently suppressed over Cu_5Pd, where the C_{N_2O} (NO conversion to N_2O, Fig. 3b and S7†) was much lower than those for Pd. Thus, the single-atom alloy catalyst enabled not only a decrease in the noble metal use to 1/10 but also highly selective NO_x removal. In the reactions conducted in the presence of O_2 and O_2 + C_3H_6, reaction temperatures greater than 200 °C were needed to achieve sufficient catalytic performance (Fig. 3 and S7†). A possible explanation is that the number of active sites for NO reduction decreased because of the involvement of other reactions such as CO and/or C_3H_6 oxidation.

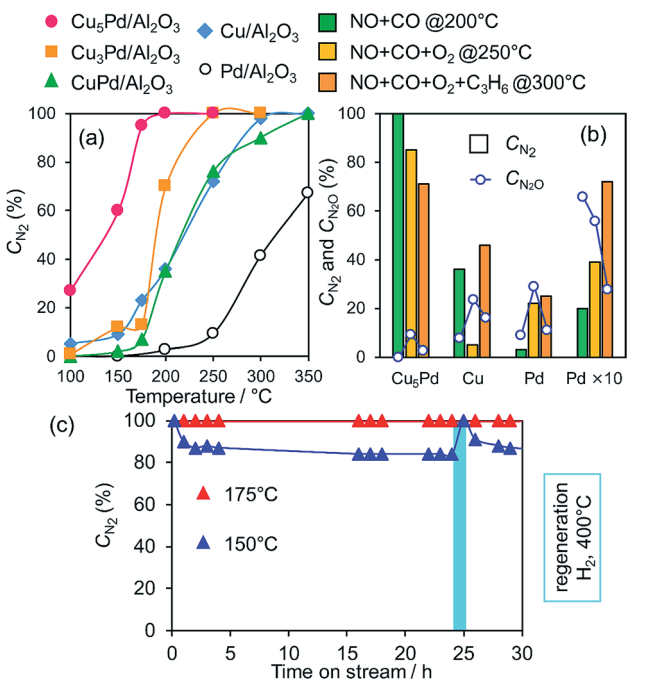

Fig. 3 (a) NO conversion to N_2 during the NO reduction by CO over Pd, Cu, and Cu–Pd catalysts as a function of reaction temperature (NO, CO: 0.5%, GHSV = 80 000 h^{-1}). (b) Comparison between C_{N_2} and C_{N_2O} in NO reduction in the presence of O_2 and C_3H_6. (c) Stability test for Cu_5Pd/Al_2O_3 in the NO + CO reaction at low temperatures (NO, CO: 0.5%, GHSV = 40 000 h^{-1}).

Next, to clarify the nature of the synergistic effect, we conducted a mechanistic study based on kinetic analysis and density functional theory (DFT) calculations. First, the apparent activation energy (E_A) for NO reduction by CO was estimated for the representative catalysts. The corresponding Arrhenius-type plots and the resulting E_A values are shown in Fig. 4 and Table 2, respectively. Cu_5Pd gave an E_A value lower than those of Pd and Cu, which is consistent with the observed catalytic activity. In addition, we estimated the reaction orders for NO and CO pressures (P_{NO} and P_{CO}, respectively) to consider the rate-determining step (RDS). Both Cu and Cu_5Pd showed negative and positive orders for P_{NO} and P_{CO}, respectively (see Table 2 and Fig. S8† for details). Unlike the case for Pd-based catalysts,[49] bond dissociation of N–O has been speculated to occur *via* $(NO)_2$ dimer formation on Cu surfaces.[50–52] Therefore, in the present study, an extended Langmuir–Hinshelwood model that includes $(NO)_2$ dimer formation, the subsequent N–O scission (N_2O formation), and N_2O decomposition (N_2 formation) was considered. We solved the rate equation of each step regarded as the RDS by using the overall site balance and equilibrium constants for the other steps (see the ESI,† kinetic analysis). In most cases, the reaction order for P_{NO} is positive, which is inconsistent with the observed experimental results. Conversely, when the N–O scission of the $(NO)_2$ is considered as the RDS, the orders for P_{NO} and P_{CO} range from −2 to 0 and from 0 to 2, respectively, in agreement with the experimental values. Thus, our kinetic study suggests that the N–O scission was the RDS in NO reduction by CO. Upon incorporation of Pd atoms into pure Cu, the order for P_{NO} becomes less negative, while that for P_{CO} decreases substantially. This result indicates that the strong adsorption of NO inhibits CO adsorption onto Cu, while the latter is enhanced in the presence of Pd. We performed DFT calculations for the relevant elemental steps on pure and Pd-doped Cu surfaces. On the basis of the literature,[53] the step site of the (211) surface was considered the active site for N–O scission (Fig. S9†). The corresponding energy diagrams are shown in Fig. 5.

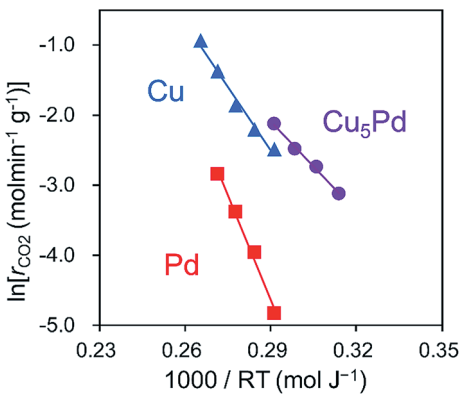

Fig. 4 Arrhenius-type plots obtained in the NO + CO reaction over Cu_5Pd/Al_2O_3, Cu/Al_2O_3, and Pd/Al_2O_3 catalysts.

Table 2 Activation energies estimated from experiments and from DFT calculations, along with reaction orders

	E_A/kJ mol^{-1} (/eV)		
	Pd	Cu	Cu_5Pd
Experiment	99.5	60.8	42.7
DFT: N–O	100.2[a]	59.8	47.9
DFT: CO + O	100.1[b]	60.9	34.1
Reaction order			
P_{NO}	—	−0.27	−0.02
P_{CO}	—	1.93	0.44

[a] NO dissociation at the step of Pd(511).[16] [b] CO oxidation on Pd(111).[16]

NO adsorption was weakened by the addition of Pd, which is consistent with the change in the reaction orders (Table 2). Dimerization occurs at the terrace site adjacent to the step site, with a negligible energy barrier. The subsequent N–O scission is triggered by capture of an oxygen atom by the edge Cu atoms, resulting in the formation of an on-top N_2O with E_A values of 59.8 and 47.9 kJ mol^{-1} for pure and Pd-doped Cu, respectively. The calculated E_A values agree with the experimental values (Table 2). The lower E_A for the Pd-doped Cu appears to originate from the destabilized adsorption of the $(NO)_2$ dimer by Pd.

We also considered the CO oxidation process (CO + O → CO_2), which is necessary for the catalytic cycle (Fig. S10†). The CO + O reaction over pure and Pd-doped Cu(111) surfaces gave E_A values of 60.9 kJ mol^{-1} and 34.1 kJ mol^{-1}, respectively (Table 2 and Fig. S10†). These values are very similar to or lower than those for N–O scission, which is consistent with the RDS being the scission of N–O. We also simulated the N_2O decomposition process (N_2O → N_2 + O) on Cu(211) and (111) surfaces to understand the intrinsic high N_2 selectivity of Cu (Fig. 6 and S11; see S12† for the pictures of the optimized structures).

The monodentate linear N_2O was bent to form a bidentate N_2O at the edge site of the Cu(211) plane without an energy barrier. The bidentate N_2O was subsequently decomposed into N_2 and O with a low E_A of 33.4 kJ mol^{-1}, indicating that the N_2O once formed could be smoothly decomposed into N_2 to afford high N_2 selectivity. Although the Cu(111) surface was also active

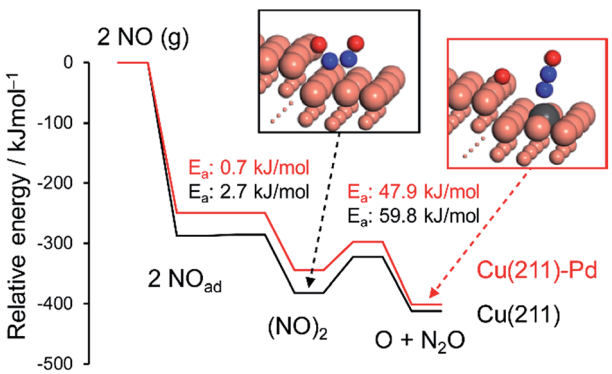

Fig. 5 Energy diagrams of NO adsorption, dimerization, and the dimer's decomposition over pure and Pd-doped Cu(211) surfaces. The total energy of the slab and free NO was set to zero.

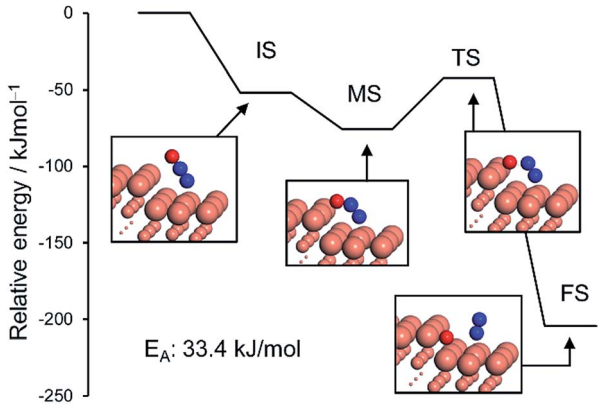

Fig. 6 Energy diagrams of N_2O bending (initial (IS) to intermediate (MS) states) and its subsequent decomposition to N_2 and O (MS to final state (FS)) over the Cu(211) surface. The total energy of slab and free N_2O was set to zero.

for N_2O decomposition in a similar fashion, the energy barrier was higher than that of Cu(211) (51.6 kJ mol^{-1}, Fig. S11†). Because large Cu–Cu ensembles are present on the surface of the Cu and Cu-rich catalysts (Cu_5Pd and Cu_3Pd), N_2O decomposition could also be enhanced on these catalysts. However, for CuPd, this effect is limited because of the dilution of Cu–Cu ensembles and the increase of Pd–Pd ensembles. Thus, our calculation rationalized the substantial enhancement in catalytic activity on the basis of the formation of the Cu–Pd single-atom alloy and the origin of the excellent selectivity for N_2 formation. The elucidated mechanism differs completely from those proposed for other bimetallic alloy systems. For example, for the Pt–Co system, Sato *et al.* reported that alloying with Co makes Pt electron-rich, which enhances back donation to adsorbed NO, inducing bond breaking.[13] Therefore, Co likely acts as a promoter for Pt. By contrast, in our system, the isolated Pd acts as an efficient promotor for Cu.

Conclusion

We prepared a series of Cu–Pd/Al_2O_3 catalysts for selective NO reduction at low temperatures. Alloying of Pd with a large amount of Cu (Cu/Pd = 5) isolates Pd and drastically improves both the catalytic activity and N_2 selectivity, affording outstanding catalytic performance. In the NO reduction by CO, NO is completely converted to N_2 even at 175 °C, with long-term stability for at least 30 h. The high catalytic performance is also achieved in the presence of O_2 and C_3H_6, where the amount of Pd needed for a comparable performance can be reduced to 1/10, with minimum evolution of N_2O. For Cu/Al_2O_3 and Cu_5Pd/Al_2O_3, the N–O bond scission of the $(NO)_2$ dimer is the RDS in NO reduction by CO. This step is kinetically facilitated by the isolated Pd atoms. N_2O decomposition to N_2 smoothly proceeds on the Cu surface, which contributes to the excellent N_2 selectivity observed for Cu and Cu-rich catalysts. The key to this efficient catalysis is the sufficient isolation of Pd atoms by Cu, highlighting the importance of catalyst design based on single-atom alloy structures. The insights gained in this study provide not only a highly efficient deNO_x system with substantially reduced noble-metal content, but also open a new path for the chemistry of single-atom alloys.

Conflicts of interest

There are no conflicts to declare.

Acknowledgements

This work was supported by JSPS KAKENHI (Grant Numbers 17H01341 and 17H04965) and by MEXT within the projects "Integrated Research Consortium on Chemical Sciences (IRCCS)" and "Elements Strategy Initiative to Form Core Research Center", as well as by the JST CREST project JPMJCR17J3. We deeply appreciate Dr H. Asakura of Kyoto University for help with XAFS measurement. We thank the technical staff of the Research Institute for Electronic Science, Hokkaido University for help with HAADF-STEM observation. Computation time was provided by the supercomputer systems at the Institute for Chemical Research, Kyoto University. X-ray absorption measurements were carried out at the BL-14B2 beamline of SPring-8 at the Japan Synchrotron Radiation Research Institute (JASRI; 2018A1757).

References

1 P. Pacher, J. S. Beckman and L. Liaudet, *Physiol. Rev.*, 2007, **87**, 315–424.
2 B. C. Berks, S. J. Ferguson, J. W. B. Moir and D. J. Richardson, *Biochim. Biophys. Acta, Bioenerg.*, 1995, **1232**, 97–173.
3 F. Rezaei, A. A. Rownaghi, S. Monjezi, R. P. Lively and C. W. Jones, *Energy Fuels*, 2015, **29**, 5467–5486.
4 C. Monn, *Atmos. Environ.*, 2001, **35**, 1–32.
5 J. H. Wang, H. Chen, Z. C. Hu, M. F. Yao and Y. D. Li, *Catal. Rev.*, 2015, **57**, 79–144.
6 J. H. Holles, R. J. Davis, T. M. Murray and J. M. Howe, *J. Catal.*, 2000, **195**, 193–206.
7 A. Srinivasan and C. Depcik, *Catal. Rev.*, 2010, **52**, 462–493.
8 J. Shibata, M. Hashimoto, K. Shimizu, H. Yoshida, T. Hattori and A. Satsuma, *J. Phys. Chem. B*, 2004, **108**, 18327–18335.
9 W. Z. An, Q. L. Zhang, K. T. Chuang and A. R. Sanger, *Ind. Eng. Chem. Res.*, 2002, **41**, 27–31.
10 R. Burch, J. P. Breen and F. C. Meunier, *Appl. Catal., B*, 2002, **39**, 283–303.
11 V. Tomasic, *Catal. Today*, 2007, **119**, 106–113.
12 S. Hosokawa, K. Matsuki, K. Tamaru, Y. Oshino, H. Aritani, H. Asakura, K. Teramura and T. Tanaka, *Mol. Catal.*, 2017, **442**, 74–82.
13 K. Sato, A. Ito, H. Tomonaga, H. Kanematsu, Y. Wada, H. Asakura, S. Hosokawa, T. Tanaka, T. Toriyama and T. Yamamoto, *ChemPlusChem*, 2019.
14 T. Tanabe, T. Imai, T. Tokunaga, S. Arai, Y. Yamamoto, S. Ueda, G. V. Ramesh, S. Nagao, H. Hirata, S. Matsumoto, T. Fujita and H. Abe, *Chem. Sci.*, 2017, **8**, 3374–3378.
15 T. Imai, S. Ueda, S. Nagao, H. Hirata, K. R. Deepthi and H. Abe, *RSC Adv.*, 2017, **7**, 9628–9631.

16 J. Jeon, K. Kon, T. Toyao, K. Shimizu and S. Furukawa, *Chem. Sci.*, 2019, **10**, 4148–4162.
17 M. V. Twigg, *Appl. Catal., B*, 2007, **70**, 2–15.
18 P. Granger, C. Dujardin, J. F. Paul and G. Leclercq, *J. Mol. Catal. A: Chem.*, 2005, **228**, 241–253.
19 G. Kyriakou, M. B. Boucher, A. D. Jewell, E. A. Lewis, T. J. Lawton, A. E. Baber, H. L. Tierney, M. Flytzani-Stephanopoulos and E. C. H. Sykes, *Science*, 2012, **335**, 1209–1212.
20 A. Wang, J. Li and T. Zhang, *Nat. Rev. Chem.*, 2018, **2**, 65.
21 M. J. Hülsey, J. Zhang and N. Yan, *Adv. Mater.*, 2018, **30**, 1802304.
22 M. T. Greiner, T. E. Jones, S. Beeg, L. Zwiener, M. Scherzer, F. Girgsdies, S. Piccinin, M. Armbruster, A. Knop-Gericke and R. Schlogl, *Nat. Chem.*, 2018, **10**, 1008–1015.
23 P. Aich, H. J. Wei, B. Basan, A. J. Kropf, N. M. Schweitzer, C. L. Marshall, J. T. Miller and R. Meyer, *J. Phys. Chem. C*, 2015, **119**, 18140–18148.
24 G. X. Pei, X. Y. Liu, A. Q. Wang, A. F. Lee, M. A. Isaacs, L. Li, X. L. Pan, X. F. Yang, X. D. Wang, Z. J. Tai, K. Wilson and T. Zhang, *ACS Catal.*, 2015, **5**, 3717–3725.
25 X. X. Cao, A. Mirjalili, J. Wheeler, W. Xie and B. W. L. Jang, *Front. Chem. Sci. Eng.*, 2015, **9**, 442–449.
26 F. R. Lucci, J. L. Liu, M. D. Marcinkowski, M. Yang, L. F. Allard, M. Flytzani-Stephanopoulos and E. C. H. Sykes, *Nat. Commun.*, 2015, **6**, 8550.
27 J. L. Liu, J. J. Shan, F. R. Lucci, S. F. Cao, E. C. H. Sykes and M. Flytzani-Stephanopoulos, *Catal. Sci. Technol.*, 2017, **7**, 4276–4284.
28 M. D. Marcinkowski, J. L. Liu, C. J. Murphy, M. L. Liriano, N. A. Wasio, F. R. Lucci, M. Flytzani-Stephanopoulos and E. C. H. Sykes, *ACS Catal.*, 2017, **7**, 413–420.
29 H. Miura, K. Endo, R. Ogawa and T. Shishido, *ACS Catal.*, 2017, **7**, 1543–1553.
30 P. Bera, K. C. Patil and M. S. Hegde, *Phys. Chem. Chem. Phys.*, 2000, **2**, 3715–3719.
31 P. Miguel, P. Granger, N. Jagtap, S. Umbarkar, M. Dongare and C. Dujardin, *J. Mol. Catal. A: Chem.*, 2010, **322**, 90–97.
32 H. Iwamoto, S. Kameoka, Y. Xu, C. Nishimura and A. P. Tsai, *J. Phys. Chem. Solids*, 2019, **125**, 64–73.
33 M. D. Segall, P. J. D. Lindan, M. J. Probert, C. J. Pickard, P. J. Hasnip, S. J. Clark and M. C. Payne, *J. Phys.: Condens. Matter*, 2002, **14**, 2717–2744.
34 D. Vanderbilt, *Phys. Rev. B: Condens. Matter Mater. Phys.*, 1990, **41**, 7892–7895.
35 J. P. Perdew, K. Burke and M. Ernzerhof, *Phys. Rev. Lett.*, 1996, **77**, 3865–3868.
36 A. Tkatchenko and M. Scheffler, *Phys. Rev. Lett.*, 2009, **102**, 073005.
37 H. J. Monkhorst and J. D. Pack, *Phys. Rev. B*, 1976, **13**, 5188–5192.
38 N. Govind, M. Petersen, G. Fitzgerald, D. King-Smith and J. Andzelm, *Comput. Mater. Sci.*, 2003, **28**, 250–258.
39 T. A. Halgren and W. N. Lipscomb, *Chem. Phys. Lett.*, 1977, **49**, 225–232.
40 W. K. Kuhn, J. Szanyi and D. W. Goodman, *Surf. Sci.*, 1992, **274**, L611–L618.
41 O. Dulaurent, X. Courtois, V. Perrichon and D. Bianchi, *J. Phys. Chem. B*, 2000, **104**, 6001–6011.
42 S. Zhou, B. Varughese, B. Eichhorn, G. Jackson and K. McIlwrath, *Angew. Chem., Int. Ed.*, 2005, **44**, 4539–4543.
43 M. Fernández-Garcia, A. Martinez-Arias, C. Belver, J. Anderson, J. Conesa and J. Soria, *J. Catal.*, 2000, **190**, 387–395.
44 F. Gao, Y. Wang and D. W. Goodman, *J. Catal.*, 2009, **268**, 115–121.
45 T. Hirano, Y. Ozawa, T. Sekido, T. Ogino, T. Miyao and S. Naito, *Catal. Commun.*, 2007, **8**, 1249–1254.
46 A. Hungrıa, A. Iglesias-Juez, A. Martınez-Arias, M. Fernández-Garcıa, J. Anderson, J. Conesa and J. Soria, *J. Catal.*, 2002, **206**, 281–294.
47 T. Komatsu, H. Kobayashi, K. Kusada, Y. Kubota, M. Takata, T. Yamamoto, S. Matsumura, K. Sato, K. Nagaoka and H. Kitagawa, *Chem.–Eur. J.*, 2017, **23**, 57–60.
48 A. Hungría, M. Fernández-García, J. Anderson and A. Martínez-Arias, *J. Catal.*, 2005, **235**, 262–271.
49 D. R. Rainer, S. M. Vesecky, M. Koranne, W. S. Oh and D. W. Goodman, *J. Catal.*, 1997, **167**, 234–241.
50 W. Brown, R. Sharma, D. King and S. Haq, *J. Phys. Chem.*, 1996, **100**, 12559–12568.
51 A. Bogicevic and K. Hass, *Surf. Sci.*, 2002, **506**, L237–L242.
52 N. Takagi, K. Ishimura, H. Miura, T. Shishido, R. Fukuda, M. Ehara and S. Sakaki, *ACS Omega*, 2019, **4**, 2596–2609.
53 R. Burch, S. Daniells and P. Hu, *J. Chem. Phys.*, 2004, **121**, 2737–2745.